

Accelerating the calculation of electron–phonon coupling strength with machine learning

Received: 6 February 2024

Yang Zhong^{1,2,3}, Shixu Liu^{1,2,3}, Binhua Zhang^{1,2}, Zhiguo Tao^{1,2}, Yuting Sun^{1,2}, Weibin Chu^{1,2}, Xin-Gao Gong^{1,2}, Ji-Hui Yang^{1,2}✉ & Hongjun Xiang^{1,2}✉

Accepted: 9 July 2024

Published online: 8 August 2024

 Check for updates

The calculation of electron–phonon couplings (EPCs) is essential for understanding various fundamental physical properties, including electrical transport, optical and superconducting behaviors in materials. However, obtaining EPCs through fully first-principles methods is notably challenging, particularly for large systems or when employing advanced functionals. Here we introduce a machine learning framework to accelerate EPC calculations by utilizing atomic orbital-based Hamiltonian matrices and gradients predicted by an equivariant graph neural network. We demonstrate that our method not only yields EPC values in close agreement with first-principles results but also enhances calculation efficiency by several orders of magnitude. Application to GaAs using the Heyd–Scuseria–Ernzerhof functional reveals the necessity of advanced functionals for accurate carrier mobility predictions, while for the large Kagome crystal CsV_3Sb_5 , our framework reproduces the experimentally observed double domes in pressure-induced superconducting phase diagrams. This machine learning framework offers a powerful and efficient tool for the investigation of diverse EPC-related phenomena in complex materials.

Electron–phonon couplings (EPCs)^{1,2} are critical in various physical phenomena such as temperature-dependent band gaps, nonradiative carrier recombination, thermal and electrical conductivity and superconductivity. In semiconductors, EPCs often dominate carrier scattering, limiting carrier mobility³. In Bardeen–Cooper–Schrieffer (BCS) superconductors⁴, EPCs induce an attractive interaction between electrons, forming Cooper pairs and enabling superconductivity. Consequently, accurately calculating EPCs is essential for understanding electron and phonon behavior in materials. Currently, density functional perturbation theory (DFPT)⁵, combined with maximally localized Wannier functions^{6,7}, is the most efficient method for calculating EPC matrix elements on dense electron and phonon wave vector grids in the Brillouin zone. DFPT-calculated perturbation potentials on coarse grids can also be converted into EPC matrices in the localized

atomic orbital (AO) basis set⁸, offering similar accuracy to the Wannier interpolation method. However, the computational cost of DFPT scales with the number of atoms (N) as $O(N^3)$, limiting its application to large systems. Moreover, DFPT currently supports only local or semi-local density functionals, which are inadequate for accurately characterizing many electronic properties, such as semiconductor band gaps. Advanced functionals, such as the Heyd–Scuseria–Ernzerhof (HSE) hybrid functional^{9,10}, are needed for precise EPC predictions, but calculating EPCs in the full Brillouin zone using hybrid functionals or GW (where G represents the single-particle Green's function, and W represents the screened Coulomb interaction) perturbation theory¹¹ is challenging due to the high computational demands in the self-consistent density functional theory (DFT) loop. This restricts EPC investigations to small systems and limits accuracy to standard

¹Key Laboratory of Computational Physical Sciences (Ministry of Education), Institute of Computational Physical Sciences, State Key Laboratory of Surface Physics, and Department of Physics, Fudan University, Shanghai, China. ²Shanghai Qi Zhi Institute, Shanghai, China. ³These authors contributed equally: Yang Zhong, Shixu Liu. ✉e-mail: jhyang04@fudan.edu.cn; hxiang@fudan.edu.cn

exchange-correlation functionals. Recently, real-space finite difference schemes within the projector-augmented wave method have been proposed for EPC calculations with the HSE functional¹². However, the necessary supercell calculations for the HSE functional are still prohibitively expensive. Additionally, a method based on singular value decomposition compresses the required EPC matrix elements but still relies on initial, computationally expensive DFPT calculations on a coarse grid¹³. To explore EPC-related properties in practical materials, methods beyond DFT are needed for efficient and accurate EPC calculations using advanced functionals.

Deep-learning tight-binding methods based on AOs have been developed to map a structure to an ab initio Hamiltonian matrix^{14–17}. For example, Hamiltonian graph neural networks (HamGNN)¹⁴ have shown accuracy in fitting electronic Hamiltonian matrices using neural networks, accelerating DFT calculations by bypassing the self-consistent loop. These methods offer potential opportunities to speed up EPC computations, but challenges remain. First, deep-learning tight-binding methods like HamGNN use nonorthogonal AOs, unlike the orthogonal maximally localized Wannier functions typically used to interpolate EPC matrix elements. This nonorthogonality must be considered when extracting EPC strengths. Second, while gradient backpropagation for scalar outputs is straightforward, computing derivatives of an entire Hamiltonian matrix with respect to atomic positions involves much higher computational complexity and memory requirements. Currently, an efficient deep-learning framework for calculating EPCs has not been established.

In this work, we develop a machine learning method to accelerate EPC calculations using our E(3)-equivariant HamGNN¹⁴. By efficiently computing the Hamiltonian and its gradients equivariantly, our method speeds up EPC calculations by several orders of magnitude, making it feasible for large systems on very dense grids. Our method can efficiently calculate EPCs with advanced functionals like HSE when trained with HSE data. We demonstrate its capability by accurately predicting the carrier mobility of GaAs using HSE functionals and the superconducting properties of large Kagome crystal CsV₃Sb₅. Our results show that the HSE functional is essential for correctly capturing the electronic structures and transport properties of GaAs, whereas standard DFT functionals underestimate the effective electron mass and overestimate carrier mobility. For CsV₃Sb₅, we successfully reproduce the double domes in its pressure-induced superconducting phase diagram^{18,19}. Besides, by calculating the EPCs in the large 2 × 2 × 1 charge density wave (CDW) superlattice of CsV₃Sb₅, we predict a superconducting transition temperature (T_c) that approximates experimental observations. Our machine learning framework provides an efficient method beyond DFT for accurately calculating EPCs, especially in large systems or those requiring advanced functionals.

Results

HamGNN-based workflow for computing electron–phonon interaction

HamGNN employs an E(3)-equivariant graph neural network to map crystal structures directly to Hamiltonian matrices, thus circumventing the computationally intensive self-consistent iterations in DFT. As illustrated in Fig. 1a, HamGNN constructs node features V_{ii} for the nodes in the central unit cell and edge features V_{ij} for interactions between these nodes and their neighbors, based on the local atomic environment. These features are then converted into the on-site Hamiltonian matrix H_{ii}^{on} and the off-site Hamiltonian matrix H_{ij}^{off} . Utilizing HamGNN, we propose an efficient framework for computing the electron–phonon interaction, as shown in Fig. 1b. As the first step, we generate a training dataset of ab initio tight-binding Hamiltonian matrices using software such as OpenMX^{20,21}, HONPAS^{22,23} or ABA-CUS^{24,25} to train a HamGNN model. If the HSE Hamiltonian matrix is used as the training set, HamGNN can predict EPCs at HSE levels. We build supercells by expanding the crystal structure under

consideration along three crystal lattice vectors and displacing the coordinate $\tau_{\kappa\sigma,0}$ of each atom κ within the central unit cell along three Cartesian directions σ ($\sigma = x, y, z$) by $\Delta\tau_{\kappa\sigma,0}$. The trained HamGNN model is subsequently employed to predict the Hamiltonian matrix of each supercell. The gradient of the Hamiltonian matrix for each atom is calculated using $\frac{\partial H}{\partial \tau_{\kappa\sigma,0}} = \frac{H(\tau_{\kappa\sigma,0} + \Delta\tau_{\kappa\sigma,0}) - H(\tau_{\kappa\sigma,0})}{\Delta\tau_{\kappa\sigma,0}}$. After obtaining the force constant matrix through DFT or neural network potential, the phonon spectrum and phonon eigenvector can be calculated using Phonopy^{26,27}. The EPC matrix under the nonorthogonal AO basis can be calculated using the formulas derived in Methods. Based on the EPC matrix, we can further calculate various properties related to electron–phonon interaction, such as electron mobility, breakdown strength and superconductivity. Since these properties are influenced exclusively by the magnitude of the EPCs, the focus is typically placed on the absolute values of the EPC matrix elements, $|g_{\mu\nu b}(\mathbf{k}, \mathbf{q})|$.

Accuracy and efficiency of HamGNN-based workflow

We validated our method for computing EPCs by assessing its accuracy and efficiency. We compute EPC values for silicon (Si) and silicon carbide (SiC) and compare them to results from DFT. The EPC matrix elements of Si and SiC, calculated using HamGNN and the first-principles method from the OpenMX package, are shown in Fig. 2a,b. Our HamGNN-based predictions closely match the results from OpenMX, confirming the accuracy of our method. The robustness of our model across different indices and variables in the EPC matrix $|g_{\mu\nu b}(\mathbf{k}, \mathbf{q})|$ is further demonstrated through error statistics discussed in Supplementary Discussion 1. Notably, the model does not require retraining for each new material. Previous work^{14,17} demonstrated this by accurately predicting Hamiltonian matrices for various carbon-based structures using a single model trained on 426 carbon allotropes. This model accurately predicted the EPC strengths for graphene and diamond without additional retraining, as shown in Fig. 2c,d. This highlights HamGNN's transferability in EPC calculations, particularly for certain material families, by eliminating the need for retraining.

To demonstrate the computational efficiency of our framework, we conducted a comparative analysis with DFT methodologies on GaAs for electron–phonon interaction at the HSE level and on CsV₃Sb₅ for superconductivity. We used the HONPAS package^{22,23} to compute the HSE Hamiltonian matrices of GaAs supercells. For CsV₃Sb₅, we employed Quantum ESPRESSO^{28,29} coupled with the electron–phonon Wannier (EPW)^{2,30} approach to calculate superconducting properties. For EPC calculations using HamGNN, we trained separate models for GaAs and CsV₃Sb₅ using the real-space Hamiltonian matrices of only 30 crystals each. Preparing the Hamiltonian matrices for the training set using DFT took 7.66 h with 64 cores for GaAs and 1.5 h with 64 cores for CsV₃Sb₅. Training the HamGNN model required 29.95 min for GaAs and 1.15 h for CsV₃Sb₅ on an NVIDIA H100 graphics processing unit. The inference time to calculate the Hamiltonian matrix gradient using the trained model was 21 s with 64 cores for GaAs and 160 s with 64 cores for CsV₃Sb₅. By comparison, the computational expenditure for determining the gradient of the HSE Hamiltonian matrix for GaAs, utilizing the finite difference technique within HONPAS, is estimated at approximately 78.3 h with 64 cores. Overall, the neural network method is nearly an order of magnitude more efficient than the DFT approach for calculating the HSE EPC strength. Given that the QE + EPW method is one of the standard approaches for calculating EPC strengths, we further analyze the computational cost savings of our machine learning workflow compared with QE + EPW at each step (Supplementary Table 1). In QE + EPW, the most substantial computational cost arises from the DFPT calculation, requiring 46,080 core hours for obtaining electron–phonon perturbation potentials. For larger systems, DFPT becomes increasingly demanding due to its poor scalability. Additional steps, like creating maximally localized Wannier function

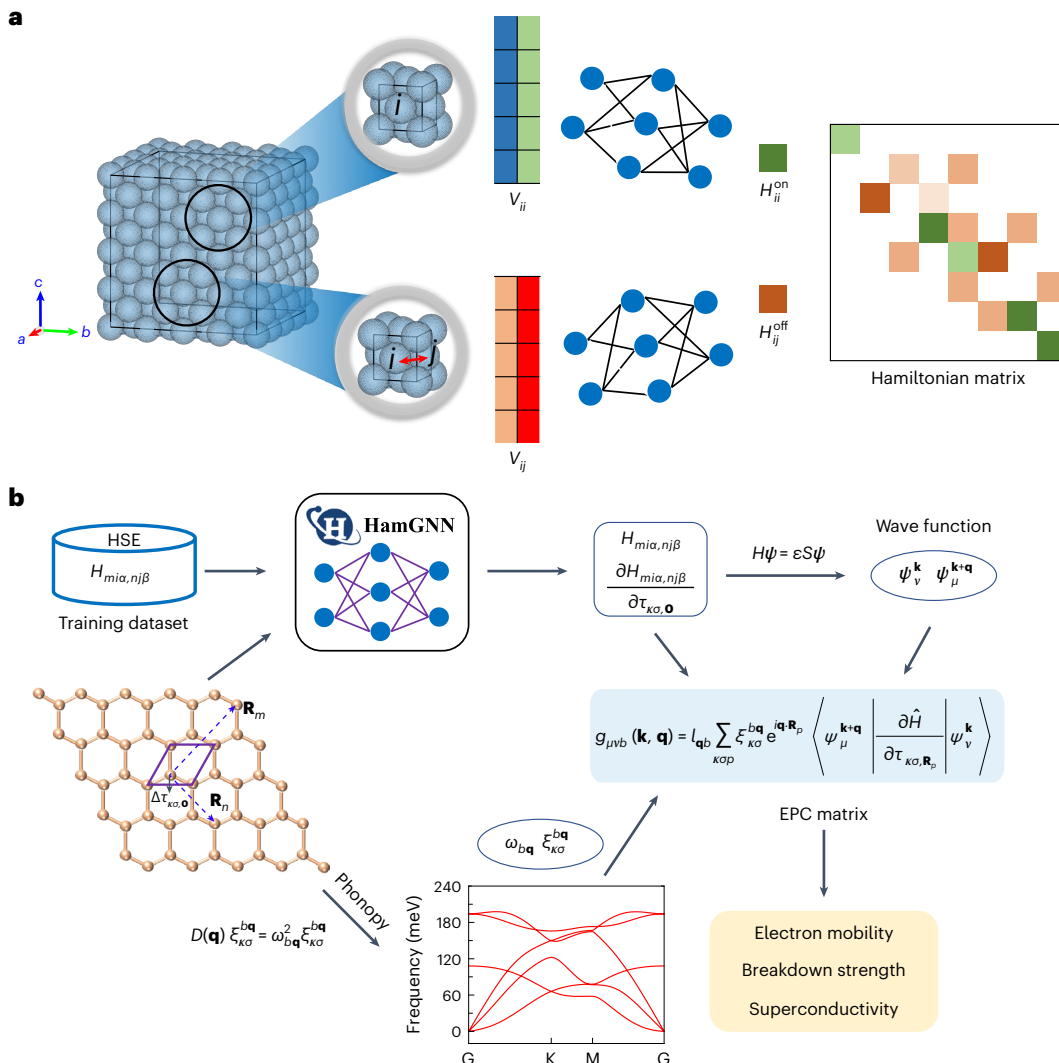


Fig. 1 | Efficient construction of Hamiltonian matrices and electron–phonon interaction framework using HamGNN. **a**, The direct mapping from crystal structure to Hamiltonian matrix using HamGNN. HamGNN employs an $E(3)$ -equivariant graph neural network to construct the Hamiltonian matrix in real-space AOIs. It constructs the node features V_{ii} for node i within the central unit cell and edge features V_{ij} for the interactions between node i and its neighboring node j based on the local atomic environment. These features are then mapped to the on-site Hamiltonian matrix H_{ii}^{on} and the off-site Hamiltonian matrix H_{ij}^{off} , corresponding to the diagonal and off-diagonal blocks of the Hamiltonian matrix, respectively. **b**, Computational framework for electron–phonon interaction using HamGNN. The model is trained on a Hamiltonian database and used to compute the Hamiltonian matrix $H_{mia,nj\beta}$ for supercells with perturbed atomic coordinates $\tau_{k\sigma,0} + \Delta\tau_{k\sigma,0}$ along the σ direction of the k th atom in the central unit cell. Here, $H_{mia,nj\beta}$ denotes the Hamiltonian element between

the α state of atom i in the unit cell at \mathbf{R}_m and the β state of atom j in the unit cell at \mathbf{R}_n . The gradient $\frac{\partial H_{mia,nj\beta}}{\partial \tau_{k\sigma,0}}$ is computed via finite difference. In the nonorthogonal AO basis, the overlap $S = \langle \phi_{mia} | \phi_{nj\beta} \rangle$ is generally nonzero for different orbitals. The Hamiltonian is diagonalized by solving the generalized eigenvalue problem $H\psi = \varepsilon S\psi$, yielding band energies ε and Bloch wave functions ψ_v^k and ψ_μ^{k+q} . Once the dynamical matrix $D(\mathbf{q})$ at each phonon wave vector \mathbf{q} is obtained from either first-principles calculations or neural network potentials, phonon frequencies $\omega_{b\mathbf{q}}$ and phonon eigenvectors $\xi_{k\sigma}^{b\mathbf{q}}$ for each phonon branch b are derived by solving $D(\mathbf{q}) \xi_{k\sigma}^{b\mathbf{q}} = \omega_{b\mathbf{q}}^2 \xi_{k\sigma}^{b\mathbf{q}}$ using Phonopy. With these quantities related to electrons and phonons, the EPC matrix $g_{\mu\nu b}(\mathbf{k}, \mathbf{q})$ can be analytically computed in the AO basis, where l_{qb} is the zero-point displacement amplitude. Detailed derivations of the formulas in the AO basis are provided in Methods.

bases and computing superconducting transition temperatures (T_c), also contribute substantially to the overall cost. Our machine learning-based framework avoids these expensive DFPT calculations, thereby greatly reducing computational time. Even considering training overhead, our workflow is considerably faster than QE + EPW. Utilizing AO bases instead of WFs offers further benefits. As AOIs are predefined analytic functions, there is no need for extra DFT calculations to choose real-space atomic bases. Furthermore, the localized nature of AOIs leads to a quicker decay of real-space electron–phonon matrix elements with increasing interatomic distance, enabling smaller supercell sizes and reducing computational load. With demonstrated accuracy and efficiency in calculating EPCs,

we now turn to demonstrate the ability of our method in predicting material properties and revealing physical mechanisms.

Carrier mobility of GaAs

GaAs was selected for electron mobility study owing to its extensive recent research. Our findings indicate that the electronic structure and electron effective mass of GaAs are highly sensitive to lattice constants and exchange-correlation functionals. The experimental lattice parameter of GaAs is 5.65 Å, while optimized values using local density approximation (LDA) and Perdew–Burke–Ernzerhof (PBE) functionals are 5.55 Å and 5.75 Å, respectively. These discrepancies lead to calculated effective masses of 0.0498 (LDA) and 0.0102 (PBE), compared

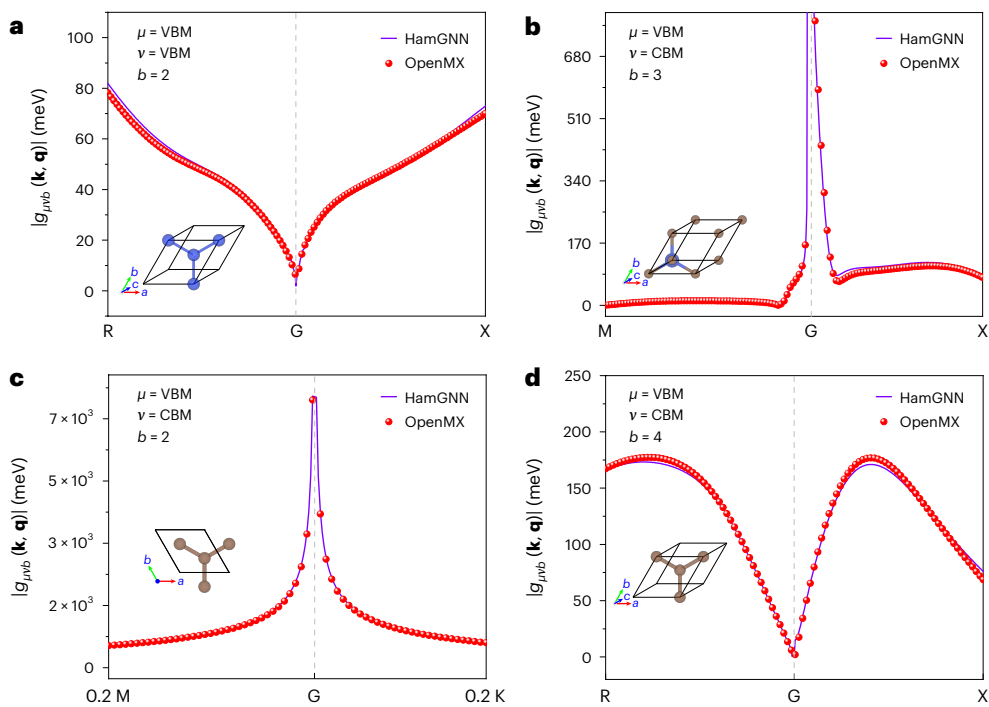


Fig. 2 | Comparison of EPC matrix elements. $|g_{\mu vb}(\mathbf{k}, \mathbf{q})|$ computed by HamGNN and DFT for selected initial states μ , final states v and phonon branches b for several materials (the \mathbf{k} point is fixed at G , while \mathbf{q} points are chosen along high-symmetry lines). **a,b**, Comparison of the predicted (solid line) EPC matrix elements for Si (**a**) and SiC (**b**) using separate HamGNN models trained on these

materials and the calculated (dotted line) values from DFT. VBM, valence band maximum; CBM, conduction band minimum. **c,d**, Comparison of the predicted (solid line) EPC matrix elements for graphene (**c**) and diamond (**d**) using a single HamGNN model trained on carbon allotropes and the calculated (dotted line) values from DFT.

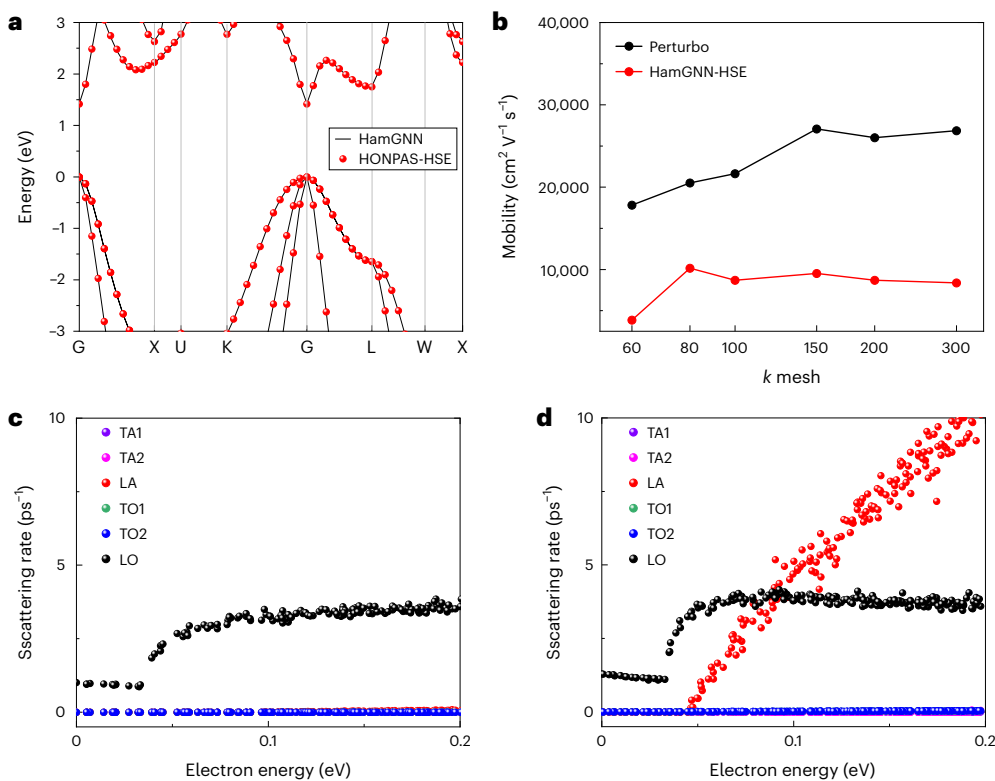
with the experimental value of 0.067. Using the experimental lattice constant, both LDA and PBE yield effective masses (0.028 and 0.029 respectively) that do not align with experimental data. Recent GaAs mobility studies^{31,32}, despite matching experimental results, often use the LDA-optimized cell, which might not accurately represent experimental conditions owing to factors such as variations in phonon spectrum and wave function across different lattice sizes. This inconsistency between electronic structure and EPCs in current GaAs mobility studies suggests that underlying physical processes may be overlooked, necessitating advanced functionals for accurate carrier mobility determination. However, this is computationally intensive, particularly for EPC calculations. Here, we address this challenge by applying our proposed EPC calculation framework to compute the carrier mobility of GaAs using the HSE functional.

We have trained a HamGNN model using the Hamiltonian matrices computed by HONPAS package under the HSE functional. Figure 3a shows a comparison between the band structures fitted by the HamGNN model and those computed using HONPAS. It demonstrates that the HamGNN model accurately captures the energy bands near Fermi level. Table 1 presents a comparison of band gap and electron effective mass calculations utilizing PBE and HSE pseudopotentials. GaAs exhibits an HSE band gap of 1.47 eV, closely approximating the experimental value of 1.43 eV, whereas PBE estimates a notably lower value of 0.52 eV. The electron effective mass under HSE is determined to be 0.069, aligning closely with the experimental measurement of 0.067, whereas PBE yields a notably lower estimate of 0.029, indicating a substantial underestimation. The electron effective mass critically influences carrier mobility in the classical Drude model, where mobility (μ) is inversely proportional to the effective mass (m^*): $\mu = \frac{qT}{m^*}$. Utilizing HSE pseudopotentials is anticipated to yield a carrier mobility closer to experimental observations compared with PBE. To validate this assertion, we independently compute GaAs's carrier mobility using both PBE and HSE pseudopotentials.

The HamGNN model was employed to calculate electron–phonon interactions and the mobility of a GaAs crystal with an experimental lattice. For comparison, we conducted DFT calculations using the QE package with PBE pseudopotentials and calculated carrier mobility with Wannier interpolation in Perturbo³³. Electron mobility values from PBE and HSE functionals are shown in Fig. 3b. A dense grid of $300 \times 300 \times 300 k$ -points was required for convergence. The predicted electron mobility at the HSE level is $8,386 \text{ cm}^2 \text{ V}^{-1} \text{ s}^{-1}$, aligning well with experimental results of $8,200$ – $8,900 \text{ cm}^2 \text{ V}^{-1} \text{ s}^{-1}$. In contrast, the PBE level yields a much higher value of $26,864 \text{ cm}^2 \text{ V}^{-1} \text{ s}^{-1}$. The discrepancy in calculated mobilities is attributed to differences in band structures near the CBM, affecting electron effective masses. To compare phonon branch contributions to carrier mobility, we calculated mode-resolved scattering rates under both PBE and HSE levels. Figure 3c,d shows that scattering rates indicate longitudinal optical (LO) phonons primarily scatter electrons near the CBM. At higher electron energies, HSE calculations reveal longitudinal acoustic (LA) phonons dominate electron scattering, unlike PBE calculations where LO phonons dominate up to 0.2 eV above the CBM. This demonstrates notable differences in electron scattering by the LA phonon mode in GaAs using different functionals. Our findings emphasize the necessity of conducting HSE-level mobility calculations, highlighting the importance of our approach due to the limitations of DFPT at this level.

Superconductivity of CsV_3Sb_5

The metallic Kagome crystal CsV_3Sb_5 has attracted considerable interest due to its CDW properties^{34,35}, superconductivity^{18,19,36–38} and Z₂ nontrivial band topology³⁶. CsV_3Sb_5 transitions to a CDW phase at $T_{\text{CDW}} = 94 \text{ K}$ and becomes superconducting below 2.5 K (ref. 34). Under high pressures, the primitive cell of CsV_3Sb_5 is dynamically stable, but at ambient pressure, it transitions to the CDW phase owing to phonon softening. X-ray diffraction and scanning tunneling microscopy reveal Star of David distortion in the CDW phase, forming a $2 \times 2 \times 1$ superlattice,



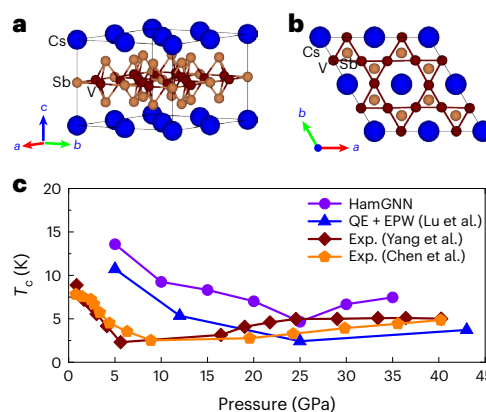
Perturbo (**c**) and HSE in HamGNN (**d**). The phonon modes include two transverse acoustic (TA) modes, one LA mode, two transverse optical (TO) modes and one LO mode. The abscissa of each scattered point represents the energy of the electronic state $|nk\rangle$.

Table 1 | Comparison of band gap and electron effective mass values between computational methods and experimental data

Method	Band gap (eV)	Electron effective mass (m_e)
QE-PBE	0.52	0.029
HONPAS-HSE	1.47	0.069
Experiment ⁴⁷	1.43	0.067

as shown in Fig. 4a,b. The competition among multiple phases in CsV_3Sb_5 leads to unique superconducting phenomena, including a double-dome structure in its pressure-dependent superconducting phase diagram. The superconducting transition temperature initially decreases with increasing pressure, disappearing around 10 GPa, then reappears and increases around 15 GPa.

Understanding the unique superconducting behavior of CsV_3Sb_5 requires accurate determination of the EPC strength across all phases. However, calculating EPCs in the CDW phase, which has a large system size (36 atoms, 492 valence electrons) and a complex band structure due to d electrons of V and Sb, is challenging with the DFPT method. The superconducting mechanism of the CDW phase remains controversial, and its relationship with various superconducting phases is not fully understood. Previous studies by Tan et al.³⁷ using deformation potential theory showed weak EPCs in the $2 \times 2 \times 1$ CDW phase of CsV_3Sb_5 , resulting in a superconducting transition temperature (T_c) as low as 0.0008 K, far below the experimental T_c of 2.5 K. The low estimated T_c may be attributed to the approximations made in the deformation potential theory³⁹, which might not accurately capture complex behaviors.



Despite some estimations using the nine-atom primitive cell, there has been no precise calculation of EPC strength for the CDW phase. To address this, we employ our proposed EPC computational framework to efficiently and accurately calculate electron–phonon interactions in both the high-pressure and CDW phases of CsV_3Sb_5 .

The T_c of CsV_3Sb_5 under various pressures was investigated using HamGNN models trained on Hamiltonian matrices of CsV_3Sb_5 supercells at different pressures, as shown in Fig. 4c. For comparison,

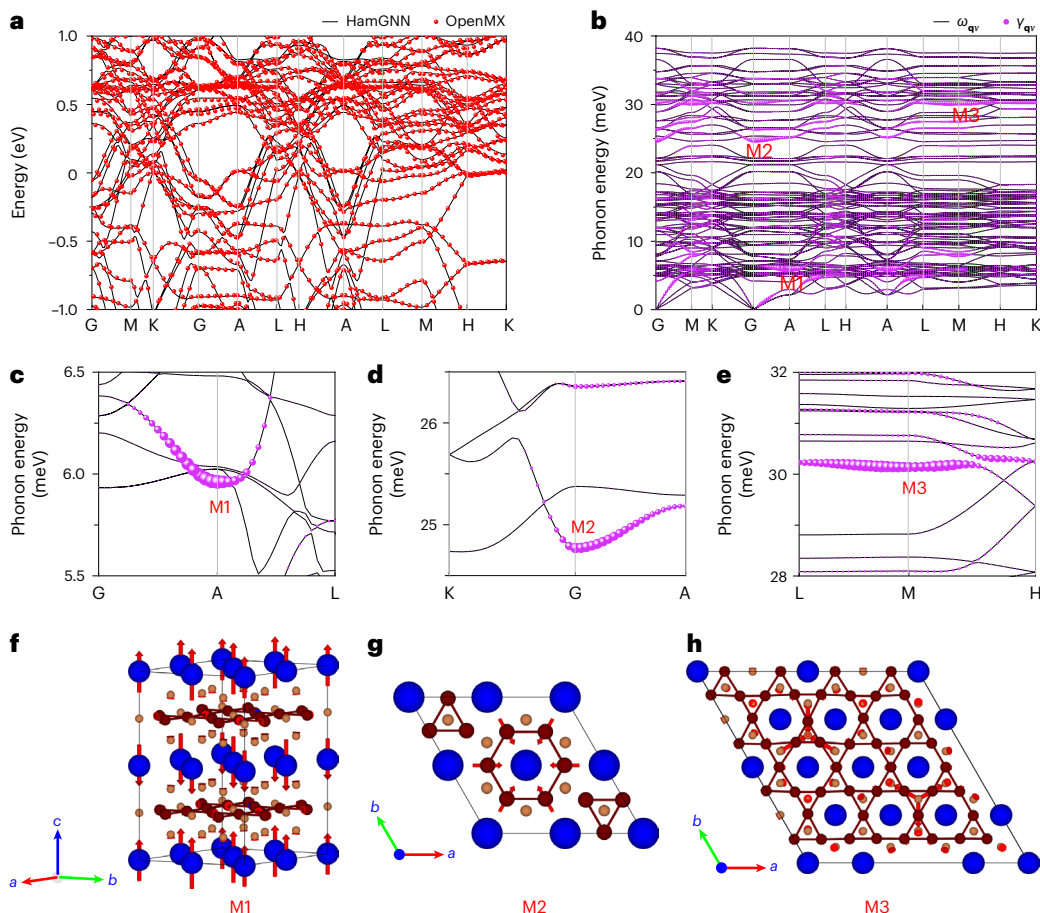


Fig. 5 | Energy bands, phonon spectrum and atomic vibration modes in the CDW phase of CsV_3Sb_5 . **a**, Comparison of the energy bands calculated by HamGNN and OpenMX. **b**, Phonon energy $\omega_{\mathbf{q}\nu}$ of the CDW phase, including moment- and mode-resolved EPC strength $y_{\mathbf{q}\nu}$ for individual phonons at each phonon wave vector \mathbf{q} and phonon branch ν , with the size of the purple dots representing the relative magnitude of $y_{\mathbf{q}\nu}$. Three vibration modes contributing

most to the EPC are identified and denoted as M1, M2 and M3. The phonon wave vectors of these modes are located near the A, Γ and M points, respectively.

c–e, Detailed phonon spectra highlighting the phonon dispersion and moment- and mode-resolved EPC strength $y_{\mathbf{q}\nu}$ in the vicinity of the three main vibration modes: mode M1 (**c**), mode M2 (**d**) and mode M3 (**e**). **f–h**, Schematic illustrations of the atomic vibration modes for mode M1 (**f**), mode M2 (**g**) and mode M3 (**h**).

T_c values from the QE + EPW method³⁸ and experimentally measured T_c values^{19,40} were included. Despite the disparities in methodologies, final relaxed high-pressure structures and pseudopotential sources utilized in OpenMX and QE software, the small discrepancies observed between the T_c predictions from the HamGNN model and QE + EPW calculations fall within an acceptable range. The HamGNN model accurately captures the T_c variation trend with pressure, consistent with QE + EPW results. Both methods reveal two distinct domes in the T_c –pressure phase diagram: the first dome shows a gradual T_c decrease up to 25 GPa, followed by a second dome with increasing T_c at higher pressures. Experimentally, T_c decreases gradually to around 10 GPa (forming the first dome) and then increases with further pressure, forming the second dome. Previous studies³⁸ have attributed discrepancies between theoretical and experimental T_c values, especially at lower pressures, to the potential existence of hidden ferromagnetic or other magnetic phases in CsV_3Sb_5 . These magnetic orders may hinder conventional superconductivity, resulting in lower observed T_c and the first superconducting dome. At higher pressures, suppression of these magnetic tendencies allows the system to recover traditional superconducting behavior, aligning theoretical and experimental T_c values in the second dome. Additionally, we calculated the phonon density of states and the Eliashberg spectral function $\alpha^2F(\omega)$ for CsV_3Sb_5 crystals under various pressures (Supplementary Fig. 7). The results indicate that increasing pressure raises the phonon frequency, shifting the phonon density of states and $\alpha^2F(\omega)$ toward higher-frequency regions.

To uncover the superconducting origin of CsV_3Sb_5 , a HamGNN model was trained using Hamiltonian matrices of CsV_3Sb_5 superlattices in the $2 \times 2 \times 1$ CDW phase. The model accurately reproduces energy bands near the Fermi surface, as shown in Fig. 5a. To calculate the EPC matrix for the CDW superlattice, we used a $3 \times 3 \times 3$ supercell containing 972 atoms. The EPC matrix elements were used to determine the T_c under various screened Coulomb repulsion constants μ_c^* , as shown in Supplementary Table 4. The estimated T_c for the CDW superlattice using BCS theory ranges from 0.262 to 0.858 K. For comparison, Tan et al.³⁷ used the empirical deformation potential method to calculate the T_c of the CDW superlattice of CsV_3Sb_5 within the BCS framework. They assumed only the breathing mode phonon branch contributes to superconductivity, resulting in a T_c of just 0.0008 K. This suggests that other neglected phonon branches may play an important role in the superconductivity of the CDW phase.

To identify the phonon modes with the largest contribution to the superconductivity of the CDW superlattice, we computed the phonon spectrum and moment- and mode-resolved EPC strength ($y_{\mathbf{q}\nu}$) for each phonon, as shown in Fig. 5b. Three specific phonon modes exert a notable influence on the superconductivity in the CDW phase (Fig. 5c–e). The M1 mode at point A corresponds to interlayer vibrations of Cs atoms (Fig. 5f), exhibiting a lower phonon frequency due to Cs's heavy mass. The M2 mode at point G and M3 mode at point M correspond to in-plane vibrations of V atoms. M2@G (Fig. 5g) involves the inverse Star of David vibration of the Kagome layer, crucial in the CDW

phase transition and competition with the superconducting phase³⁷. M3@M (Fig. 5h) represents a higher-frequency vibration mode of V Kagome layers, the contribution of which to the superconductivity of the CDW phase has not been reported in previous literature. Unlike M2@G, M3@M involves vibrations of V triangles centered on Sb atoms, resulting in higher vibrational frequency due to stronger V–Sb interactions. Our analysis suggests that the superconductivity of the CDW phase of CsV_3Sb_5 may not be attributed to the breathing mode. The estimated T_c is still lower than the experimental T_c of 2.5 K, probably due to BCS theory limitations in describing superconducting properties of CsV_3Sb_5 , warranting exploration with advanced functionals in the future.

Discussion

By examining the mobility of GaAs using hybrid functionals and the superconductivity properties of Kagome crystal CsV_3Sb_5 , we demonstrate the efficacy of our proposed machine learning method for calculating EPCs. This method is anticipated to offer a feasible solution for addressing previously intractable problems. Current studies on transport properties, such as intrinsic mobility and breakdown strength, utilizing first-principles calculation methods to fully account for EPCs, are constrained to systems comprising only several atoms owing to prohibitive computational costs. Our approach, however, is capable of handling systems with tens of atoms, representing at least an order of magnitude increase in system size. This advancement facilitates accurate studies of alloy and defect effects on semiconductor transport properties, which is crucial for the design and optimization of semiconductor devices.

Furthermore, our approach has substantial implications for understanding correlation effects on superconductivity properties. Recently, Li et al. developed GW perturbation theory¹¹ methods to reevaluate the superconductivity of systems with 3d electrons, discovering that these systems could exhibit conventional superconductivity. Our framework can achieve similar results at a markedly reduced computational expense by utilizing tens of GW calculations as the training dataset for machine learning to fit the corresponding Hamiltonian matrix. Additionally, our method enables the efficient theoretical study of various nonadiabatic properties, such as EPC-contributed thermal conductivity, the Debye–Waller effect⁴¹ and nonradiative carrier recombination⁴².

Lastly, we propose several potential improvements to our method. First, the AO basis currently adopted in our framework lacks completeness. This could be enhanced by employing more accurate triple-zeta polarized basis sets or by projecting the training datasets based on plane-wave basis onto the AO basis. Second, as system size increases, the number of AOs and, consequently, the size of the Hamiltonian matrix also increase, which may limit efficiency. This issue can be mitigated by transforming the AO basis to the Wannier function basis. Third, the cost associated with the data training process can be greatly reduced by utilizing pretrained models or our recently developed universal Hamiltonian model¹⁷.

Methods

The formalism of electron–phonon interactions using AOs

The transition amplitude from the Bloch wave function ψ_v^k with band index v and crystal momentum \mathbf{k} to the Bloch wave function ψ_μ^{k+q} with band index μ and crystal momentum $\mathbf{k} + \mathbf{q}$ is defined as the EPC matrix $g_{\mu vb}(\mathbf{k}, \mathbf{q})$ (ref. 1),

$$g_{\mu vb}(\mathbf{k}, \mathbf{q}) = \langle \psi_\mu^{k+q} | \partial_{bq} \hat{H} | \psi_v^k \rangle, \quad (1)$$

which is mediated by the emission or absorption of phonons with branch index b and crystal momentum \mathbf{q} . Substituting the perturbed Hamiltonian $\partial_{bq} \hat{H} = l_{qb} \sum_{\kappa\sigma} \xi_{\kappa\sigma}^{b\mathbf{q}} e^{i\mathbf{q}\cdot\mathbf{R}_p} \frac{\partial \hat{H}}{\partial \tau_{\kappa\sigma,\mathbf{R}_p}}$ into equation (1) yields

$$g_{\mu vb}(\mathbf{k}, \mathbf{q}) = l_{qb} \sum_{\kappa\sigma} \xi_{\kappa\sigma}^{b\mathbf{q}} e^{i\mathbf{q}\cdot\mathbf{R}_p} \left\langle \psi_\mu^{k+q} \left| \frac{\partial \hat{H}}{\partial \tau_{\kappa\sigma,\mathbf{R}_p}} \right| \psi_v^k \right\rangle, \quad (2)$$

where $l_{qb} = \sqrt{\hbar/(2\omega_{qb} \sum_{\kappa\sigma} m_\kappa \xi_{\kappa\sigma}^{b\mathbf{q}*} \xi_{\kappa\sigma}^{b\mathbf{q}})}$ is the zero-point displacement amplitude, m_κ is the mass of the κ th atom, ω_{qb} is the phonon eigenvalue, $\xi_{\kappa\sigma}^{b\mathbf{q}}$ is the component of the normalized eigenvector of the phonons with branch index b and crystal momentum \mathbf{q} at the κ th atom along the direction σ ($\sigma = x, y, z$). $\tau_{\kappa\sigma,\mathbf{R}_p}$ is the σ coordinate component of the κ th atom in the unit cell with displacement \mathbf{R}_p ($p = 1, 2, \dots, N_p$) to the central unit cell.

The electron wave function can be expanded using a set of non-orthogonal real-space AOs:

$$|\psi_v^k\rangle = \frac{1}{\sqrt{N}} \sum_{n'}^N e^{i\mathbf{R}_{n'} \cdot \mathbf{k}} \sum_{j\beta} C_{j\beta}^{k,v} \phi_{n'j\beta}, \quad (3)$$

where $C_{j\beta}^{k,v}$ is the expansion coefficient in front of the AO $\phi_{n'j\beta} \equiv \phi_{j\beta}(\mathbf{r} - \mathbf{r}_j - \mathbf{R}_{n'})$ in real space, and N is the number of unit cells in a large supercell representing Born–von Karman periodic boundary conditions. By substituting equation (3) into equation (2), the EPC matrix element, which is represented by the basis of AOs in real space, can be expressed as

$$g_{\mu vb}(\mathbf{k}, \mathbf{q}) = \frac{l_{qb}}{N} \sum_{m'n'p} \sum_{iaj\beta} \sum_{\kappa\sigma} \xi_{\kappa\sigma}^{b\mathbf{q}} e^{i\mathbf{q}\cdot\mathbf{R}_p} e^{-i\mathbf{R}_{m'} \cdot (\mathbf{k} + \mathbf{q})} e^{i\mathbf{R}_{n'} \cdot \mathbf{k}} C_{ia}^{k+q,\mu*} C_{j\beta}^{k,v} \left\langle \phi_{m'ia} \left| \frac{\partial \hat{H}}{\partial \tau_{\kappa\sigma,\mathbf{R}_p}} \right| \phi_{n'j\beta} \right\rangle. \quad (4)$$

By setting $\mathbf{R}_{m'} = \mathbf{R}_m + \mathbf{R}_p$ and $\mathbf{R}_{n'} = \mathbf{R}_n + \mathbf{R}_p$, we can derive the following equation from the translational symmetry of the crystal:

$$\left\langle \phi_{m'ia} \left| \frac{\partial \hat{H}}{\partial \tau_{\kappa\sigma,\mathbf{R}_p}} \right| \phi_{n'j\beta} \right\rangle = \left\langle \phi_{mia} \left| \frac{\partial \hat{H}}{\partial \tau_{\kappa\sigma,\mathbf{R}_p}} \right| \phi_{nj\beta} \right\rangle. \quad (5)$$

Substituting equation (5) into equation (4) can simplify the EPC matrix element calculation formula in the supercell setup as

$$g_{\mu vb}(\mathbf{k}, \mathbf{q}) = l_{qb} \sum_{mn} \sum_{iaj\beta} \sum_{\kappa\sigma} \xi_{\kappa\sigma}^{b\mathbf{q}} e^{-i(\mathbf{k}+\mathbf{q}) \cdot \mathbf{R}_m} e^{i\mathbf{k} \cdot \mathbf{R}_n} C_{ia}^{k+q,\mu*} C_{j\beta}^{k,v} \left\langle \phi_{mia} \left| \frac{\partial \hat{H}}{\partial \tau_{\kappa\sigma,\mathbf{R}_p}} \right| \phi_{nj\beta} \right\rangle. \quad (6)$$

According to the above equation, the essence of EPC matrix elements lies in calculating the matrix elements of the gradient of the Hamiltonian matrix with respect to the atomic coordinates in the central unit cell $\langle \phi_{mia} | \frac{\partial \hat{H}}{\partial \tau_{\kappa\sigma,\mathbf{R}_p}} | \phi_{nj\beta} \rangle$. Below, we provide a method to calculate this matrix element in nonorthogonal AO bases.

In the nonorthogonal AO basis, the Hamiltonian operator in real space can be expressed as

$$\hat{H} = \sum_{m'n'i'j'\alpha'\beta'} \tilde{H}_{m'i'\alpha', n'j'\beta'} |\phi_{m'i'\alpha'}\rangle \langle \phi_{n'j'\beta'}|. \quad (7)$$

Based on $\langle \phi_{mia} | \hat{H} | \phi_{nj\beta} \rangle = H_{mia,nj\beta}$, it can be inferred that $\tilde{H}_{m'i'\alpha', n'j'\beta'}$ is the matrix element of $\tilde{H} = S^{-1}HS^{-1}$, where $S_{mia,nj\beta} = \langle \phi_{mia} | \phi_{nj\beta} \rangle$ is the overlap matrix. According to equation (7), the matrix elements of the gradient of the Hamiltonian matrix with respect to the atomic coordinates $\tau_{\kappa,0}$ in the central unit cell are

$$\begin{aligned} \langle \phi_{mia} | \nabla_{\tau_{\kappa,0}} \hat{H} | \phi_{nj\beta} \rangle &= \sum_{m'n'i'j'\alpha'\beta'} \left\{ \nabla_{\tau_{\kappa,0}} \tilde{H}_{m'i'\alpha', n'j'\beta'} S_{mia,m'i'\alpha'} S_{n'j'\beta', nj\beta} \right. \\ &\quad + \tilde{H}_{m'i'\alpha', n'j'\beta'} \langle \phi_{mia} | \nabla_{\tau_{\kappa,0}} \phi_{m'i'\alpha'} \rangle S_{n'j'\beta', nj\beta} \\ &\quad \left. + \tilde{H}_{m'i'\alpha', n'j'\beta'} S_{mia,m'i'\alpha'} \langle \nabla_{\tau_{\kappa,0}} \phi_{n'j'\beta'} | \phi_{nj\beta} \rangle \right\}. \end{aligned} \quad (8)$$

To simplify equation (8) further, we first define two auxiliary matrices $A_{mia,m'i'a'}^\kappa$ and $B_{n'j'\beta',nj\beta}^\kappa$ as

$$A_{mia,m'i'a'}^\kappa = \begin{cases} \langle \phi_{0ia} | \nabla_{\tau_{i,0}} \phi_{0ia'} \rangle & \tau_{\kappa,0} = \tau_{i'} + \mathbf{R}_{m'} = \tau_i + \mathbf{R}_m \\ 0 & \tau_{\kappa,0} = \tau_{i'} + \mathbf{R}_{m'} \neq \tau_i + \mathbf{R}_m \\ -\nabla_{\tau_{i,0}} S_{mia,m'i'a'} & \tau_{\kappa,0} \neq \tau_{i'} + \mathbf{R}_{m'} \end{cases} \quad (9)$$

$$B_{n'j'\beta',nj\beta}^\kappa = \begin{cases} \langle \nabla_{\tau_{j,0}} \phi_{0jb} | \phi_{0jb'} \rangle & \tau_{\kappa,0} = \tau_{j'} + \mathbf{R}_{n'} = \tau_j + \mathbf{R}_n \\ 0 & \tau_{\kappa,0} = \tau_{j'} + \mathbf{R}_{n'} \neq \tau_j + \mathbf{R}_n \\ -\nabla_{\tau_{j,0}} S_{n'j'\beta',nj\beta} & \tau_{\kappa,0} \neq \tau_{j'} + \mathbf{R}_{n'} \end{cases} \quad (10)$$

According to equations (9) and (10), the two following equations can be obtained:

$$\langle \phi_{mia} | \nabla_{\tau_{i,0}} \phi_{m'i'a'} \rangle = \nabla_{\tau_{i,0}} S_{mia,m'i'a'} + A_{mia,m'i'a'}^\kappa \quad (11)$$

$$\langle \nabla_{\tau_{i,0}} \phi_{njb} | \phi_{nj\beta} \rangle = \nabla_{\tau_{i,0}} S_{nj\beta,nj\beta} + B_{nj\beta,nj\beta}^\kappa \quad (12)$$

According to the derivative rules of matrices, the gradient of the matrix $\tilde{H} = S^{-1}HS^{-1}$ with respect to $\tau_{\kappa,0}$ is expanded as

$$\nabla_{\tau_{i,0}} \tilde{H} = -S^{-1}(\nabla_{\tau_{i,0}} S)S^{-1}HS^{-1} + S^{-1}(\nabla_{\tau_{i,0}} H)S^{-1} - S^{-1}HS^{-1}(\nabla_{\tau_{i,0}} S)S^{-1}. \quad (13)$$

By substituting equations (12) and (13) back into equation (8), the matrix element of the gradient of the Hamiltonian matrix in the basis set of nonorthogonal AOs can be simplified to

$$\langle \phi_{mia} | \nabla_{\tau_{i,0}} \tilde{H} | \phi_{nj\beta} \rangle = [\nabla_{\tau_{i,0}} H + A^\kappa S^{-1}H + HS^{-1}B^\kappa]_{mia,nj\beta}. \quad (14)$$

Since the AO basis is known, we can analytically compute $A_{mia,m'i'a'}^\kappa$ and $B_{n'j'\beta',nj\beta}^\kappa$ without DFT calculations. Therefore, obtaining the Hamiltonian matrix H and its gradient $\frac{\partial H}{\partial \tau_{i,0}}$ is sufficient for calculating the EPC matrix element $g_{\mu\nu b}(\mathbf{k}, \mathbf{q})$ using equations (6) and (14).

Details of EPC calculations for Si, SiC, graphene and diamond using HamGNN

We constructed 100 supercells of Si and 100 supercells of SiC, each with a size of $3 \times 3 \times 3$, and computed their Hamiltonian matrices using OpenMX. These matrices were subsequently divided into training, validation and test sets in a ratio of 0.8:0.1:0.1. The HamGNN model exhibited mean absolute errors (MAEs) of 0.15 meV and 0.79 meV on the test sets for Si and SiC, respectively, demonstrating good agreement with DFT calculations (Supplementary Fig. 1). Subsequently, we employed the trained HamGNN model to compute the Hamiltonian matrices for $5 \times 5 \times 5$ supercells of Si and SiC, where the atoms in the central cell were displaced by 0.01 Å along the x , y and z directions. The gradients of the Hamiltonian matrices were derived using finite difference calculations based on the Hamiltonian matrices of these supercells. For predicting the EPC strengths in graphene and diamond, we utilized a previously trained HamGNN model based on 426 different carbon allotrope structures. To calculate the gradients of the real-space Hamiltonian matrices with respect to atomic coordinates, $7 \times 7 \times 1$ graphene supercells and $5 \times 5 \times 5$ diamond supercells were utilized, with each atom in the central cell displaced by 0.01 Å along each axis.

Details of mobility calculation for GaAs

We calculated the Hamiltonian matrices for 30 GaAs supercells with dimensions of $2 \times 2 \times 2$ using the HSE functional within the HONPAS^{22,23} package. These supercells were constructed by expanding the experimental primitive cell of GaAs, and each atom was randomly perturbed

by 0.02 Å. The Hamiltonian matrices were subsequently divided into training, validation and testing sets in a ratio of 0.8:0.1:0.1, respectively. The trained HamGNN model achieved an MAE of 0.225 meV on the test set. Subsequently, we constructed a series of $5 \times 5 \times 5$ supercells, in which the atoms in the central unit cell were displaced along each Cartesian axis by 0.01 Å. We then utilized the trained HamGNN model to predict the Hamiltonian matrix for each supercell and compute the gradient of the real-space Hamiltonian matrix using the finite difference method. The phonon eigenvalues and eigenvectors were obtained using Phonopy, based on the force constant matrix derived from HSE calculations of VASP. Given that GaAs is a polar material, the calculated EPC matrix obtained by this real-space interpolation scheme only includes local contributions. Therefore, a correction for long-range dipole interactions on the EPC is necessary, as it primarily affects the EPC matrix elements at $\mathbf{q} \rightarrow 0$. The long-range correction for the EPC matrix can be calculated analytically using the following formula^{1,2}:

$$g_{\mu\nu b}^L(\mathbf{k}, \mathbf{q}) = i \frac{4\pi}{\Omega} \frac{e^2}{4\pi\epsilon_0} \sum_\kappa \left(\frac{\hbar}{2m_\kappa \omega_{\mathbf{q}\nu}} \right)^{\frac{1}{2}} \times \sum_{\mathbf{G} \neq -\mathbf{q}} \frac{(\mathbf{q} + \mathbf{G}) \cdot \mathbf{Z}_\kappa \cdot \mathbf{Z}_\kappa^{*\mathbf{G}}}{(\mathbf{q} + \mathbf{G}) \cdot \mathbf{e}^\infty \cdot (\mathbf{q} + \mathbf{G})} \times \langle \psi_\mu^{\mathbf{k}+\mathbf{q}} | e^{i(\mathbf{q} + \mathbf{G}) \cdot (\mathbf{r} - \mathbf{r}_\kappa)} | \psi_\nu^{\mathbf{k}} \rangle, \quad (15)$$

where \mathbf{Z}_κ^* and \mathbf{e}^∞ denote the Born effective charge tensors and electron permittivity tensor, respectively, and \mathbf{G} is the reciprocal lattice vector.

To calculate the mobility, we first determine the scattering rate using the following expression³³:

$$\frac{1}{\tau_{nk}} = \frac{2\pi}{\hbar} \sum_{m\mathbf{q}n} |g_{mnv}(\mathbf{k}, \mathbf{q})|^2 \left[(1 - f_{mk+q}^0 + n_{qv}) \delta(\epsilon_{nk} - \epsilon_{mk+q} - \hbar\omega_{qv}) \right. \\ \left. + (f_{mk+q}^0 + n_{qv}) \delta(\epsilon_{nk} - \epsilon_{mk+q} + \hbar\omega_{qv}) \right], \quad (16)$$

where the summation encompasses all scattering processes from the initial state $|nk\rangle$ to the final state $|mk+q\rangle$ through a phonon $|\mathbf{q}\nu\rangle$. Here, ϵ_{nk} denotes the eigenenergy of the Kohn–Sham state $|nk\rangle$ and $\hbar\omega_{qv}$ represents the eigenenergy of the phonon. The term f_{mk+q}^0 is the Fermi–Dirac occupation of the state $|mk+q\rangle$, while n_{qv} is the Bose–Einstein occupation of the phonon $|\mathbf{q}\nu\rangle$. In this study, the temperature is fixed at 300 K for the calculation of state occupations. The delta functions ensure energy conservation during the scattering processes. Subsequently, we compute the electron mobilities under the relaxation time approximation. The mobility matrix is given by

$$\mu_{\alpha\beta} = -\frac{1}{V_{uc} n_c} \sum_{nk} \frac{\partial f_{nk}^0}{\partial \epsilon_{nk}} v_{nk,\alpha} v_{nk,\beta} \tau_{nk}, \quad (17)$$

where α and β represent the three Cartesian directions, V_{uc} is the volume of the unit cell and n_c is the carrier density. The summation over nk includes all initial states, and $v_{nk,\alpha}$ denotes the band velocity of the state $|nk\rangle$ in the α direction.

Following the methodology outlined by Zhou et al.³¹, we decompose the EPC into a long-range part and a short-range part as

$$g_{mnv}(\mathbf{k}, \mathbf{q}) = g_{mnv}^L(\mathbf{k}, \mathbf{q}) + g_{mnv}^S(\mathbf{k}, \mathbf{q}). \quad (18)$$

Consequently, the scattering rate can be partitioned into two distinct parts: the polar part and the remaining part, represented by

$$\left[\frac{1}{\tau_{nk}} \right]_{\text{Polar}} = \frac{2\pi}{\hbar} \sum_{q,m,v} |g_{mnv}^L(\mathbf{k}, \mathbf{q})|^2 F_{mnv}(\mathbf{k}, \mathbf{q}) \quad (19)$$

$$\left[\frac{1}{\tau_{nk}} \right]_{\text{Remainder}} = \frac{2\pi}{\hbar} \sum_{q,m,v} [|g_{mnv}(\mathbf{k}, \mathbf{q})|^2 - |g_{mnv}^L(\mathbf{k}, \mathbf{q})|^2] F_{mnv}(\mathbf{k}, \mathbf{q}), \quad (20)$$

where

$$F_{mnv}(\mathbf{k}, \mathbf{q}) = (1 - f_{m\mathbf{k}+\mathbf{q}}^0 + n_{qv}) \delta(\epsilon_{nk} - \epsilon_{m\mathbf{k}+\mathbf{q}} - \hbar\omega_{qv}) + (f_{m\mathbf{k}+\mathbf{q}}^0 + n_{qv}) \delta(\epsilon_{nk} - \epsilon_{m\mathbf{k}+\mathbf{q}} + \hbar\omega_{qv}). \quad (21)$$

To ensure effective convergence of the integration results on the \mathbf{q} grid, we utilize Monte Carlo integration with importance sampling. Considering that intra-valley scattering in the Gamma valley predominantly influences mobility in GaAs, we sample \mathbf{q} points using a Cauchy distribution defined as

$$f(x) = \frac{1}{\pi} \frac{\gamma}{x^2 + \gamma^2}, \quad (22)$$

where we set $\gamma = 0.035$ for the polar part as suggested by Zhou et al.³¹, and $\gamma = 0.07$ for the remainder part. As illustrated in Fig. 3b, convergence of mobility is observed at a \mathbf{k} grid size of $300 \times 300 \times 300$, utilizing 5×10^6 and 5×10^5 random \mathbf{q} points for the polar and remainder parts, respectively. The Monte Carlo sampling method enables the mobility calculations to converge with far fewer \mathbf{q} -points compared with the uniform grid method, as discussed in Supplementary Discussion 2.

Details of superconductivity calculation for CsV_3Sb_5

We employed the PBE functionals within VASP^{43,44} to optimize the structure of CsV_3Sb_5 crystals under various high pressures and the $2 \times 2 \times 1$ CDW phase of CsV_3Sb_5 at zero pressure, with a force convergence criterion set to 1×10^{-7} eV Å⁻¹. Van der Waals force corrections were incorporated using the DFT-D3 method. For the CsV_3Sb_5 crystal under high pressure, we utilized a $12 \times 12 \times 8$ k -point grid and conducted phonon spectrum calculations using a $3 \times 3 \times 2$ supercell. For the CDW superlattice with dimensions of $2 \times 2 \times 1$, structural optimization was performed on a $6 \times 6 \times 8$ k -point grid, and the phonon spectrum was calculated using a $2 \times 2 \times 2$ supercell.

Separate HamGNN models were trained for the relaxed structure of CsV_3Sb_5 at each pressure condition. To construct the training datasets, the crystal structure of CsV_3Sb_5 under each pressure was expanded into $2 \times 2 \times 2$ supercells, with each atom's coordinates randomly perturbed by 0.02 Å. We utilized OpenMX with the PBE pseudopotential to calculate Hamiltonian matrices for 30 perturbed supercells at each pressure. Each dataset was subsequently divided into training, validation and test sets in a ratio of 0.8:0.1:0.1. Separate HamGNN models were then trained for the structures at each pressure, achieving an average MAE of 1.72 meV on the test sets. The energy bands predicted by these HamGNN models match well with those calculated by DFT for CsV_3Sb_5 crystals under various pressures, as shown in Supplementary Fig. 6. Additionally, we constructed a series of $3 \times 3 \times 3$ CsV_3Sb_5 supercells, with atoms in the central unit cell displaced by 0.01 Å along each Cartesian coordinate axis. The trained HamGNN models were employed to predict the real-space Hamiltonian matrices for each supercell, and the gradients were computed using the finite difference method. The EPC matrix elements were obtained by leveraging the gradient of the real-space Hamiltonian in conjunction with the phonon spectrum. These EPC matrix elements were subsequently used to calculate T_c .

The superconducting transition temperature T_c is estimated using the Allen–Dynes-modified McMillan formula¹:

$$T_c = \frac{\omega_{\log}}{1.2} \exp\left(-\frac{1.04(1+\lambda)}{\lambda - \mu_c^*(1+0.62\lambda)}\right), \quad (23)$$

where μ_c^* is the Coulomb pseudopotential, taken as 0.12 in our calculation^{37,38}. The logarithmic average of phonon frequencies, ω_{\log} , is defined as

$$\omega_{\log} = \exp\left[\frac{2}{\lambda} \int_0^\infty \frac{\alpha^2 F(\omega)}{\omega} \log(\omega) d\omega\right]. \quad (24)$$

In this expression, $\alpha^2 F(\omega)$ represents the Eliashberg spectral function

$$\alpha^2 F(\omega) = \frac{1}{2\pi N(\epsilon_F)} \sum_{v,\mathbf{q}} \frac{\gamma_{qv}}{\omega_{qv}} \delta(\omega - \omega_{qv}). \quad (25)$$

The phonon linewidth, γ_{qv} , can be calculated using

$$\gamma_{qv} = 2\pi\omega_{qv} \sum_{nm,\mathbf{k}} |g_{mnv}(\mathbf{k}, \mathbf{q})|^2 \delta(\epsilon_{nk} - \epsilon_F) \delta(\epsilon_{m\mathbf{k}+\mathbf{q}} - \epsilon_F), \quad (26)$$

where $N(\epsilon_F)$ is the density of states near the Fermi energy ϵ_F . The total EPC constant λ is computed as

$$\lambda = 2 \int_0^\infty \frac{\alpha^2 F(\omega)}{\omega} d\omega. \quad (27)$$

These equations collectively allow for the determination of the superconducting transition temperature T_c .

Data availability

The Hamiltonian and Hamiltonian gradient data, generated by HamGNN, are available on Zenodo at <https://doi.org/10.5281/zenodo.1120426> (ref. 45) for calculating the carrier mobility of GaAs and the superconducting transition temperature of CsV_3Sb_5 . Source data are provided with this paper.

Code availability

The code for calculating the mobility and superconductivity is available on GitHub (<https://github.com/QuantumLab-ZY/HamEPC>) and Zenodo at <https://doi.org/10.5281/zenodo.1268594> (ref. 46).

References

- Giustino, F. Electron–phonon interactions from first principles. *Rev. Mod. Phys.* **89**, 015003 (2017).
- Lee, H. et al. Electron–phonon physics from first principles using the EPW code. *NPJ Comput. Mater.* **9**, 156 (2023).
- Brunin, G. et al. Phonon-limited electron mobility in Si, GaAs, and GaP with exact treatment of dynamical quadrupoles. *Phys. Rev. B* **102**, 094308 (2020).
- Bardeen, J., Cooper, L. N. & Schrieffer, J. R. Theory of superconductivity. *Phys. Rev.* **108**, 1175–1204 (1957).
- Baroni, S., de Gironcoli, S., Dal Corso, A. & Giannozzi, P. Phonons and related crystal properties from density-functional perturbation theory. *Rev. Mod. Phys.* **73**, 515–562 (2001).
- Giustino, F., Cohen, M. L. & Louie, S. G. Electron–phonon interaction using Wannier functions. *Phys. Rev. B* **76**, 165108 (2007).
- Marzari, N., Mostofi, A. A., Yates, J. R., Souza, I. & Vanderbilt, D. Maximally localized Wannier functions: theory and applications. *Rev. Mod. Phys.* **84**, 1419–1475 (2012).
- Agapito, L. A. & Bernardi, M. Ab initio electron–phonon interactions using atomic orbital wave functions. *Phys. Rev. B* **97**, 235146 (2018).
- Heyd, J., Scuseria, G. E. & Ernzerhof, M. Hybrid functionals based on a screened Coulomb potential. *J. Chem. Phys.* **118**, 8207–8215 (2003).
- Heyd, J., Scuseria, G. E. & Ernzerhof, M. Erratum: “Hybrid functionals based on a screened Coulomb potential” [J. Chem. Phys. 118, 8207 (2003)]. *J. Chem. Phys.* **124**, 219906 (2006).
- Li, Z., Antonius, G., Chan, Y.-H. & Louie, S. G. Electron–phonon coupling from GW perturbation theory: practical workflow combining BerkeleyGW, ABINIT, and EPW. *Comp. Phys. Commun.* **295**, 109003 (2024).

12. Engel, M., Marsman, M., Franchini, C. & Kresse, G. Electron-phonon interactions using the projector augmented-wave method and Wannier functions. *Phys. Rev. B* **101**, 184302 (2020).
13. Luo, Y., Desai, D., Chang, B. K., Park, J. & Bernardi, M. Data-driven compression of electron-phonon interactions. *Phys. Rev. X* **14**, 021023 (2024).
14. Zhong, Y., Yu, H., Su, M., Gong, X. & Xiang, H. Transferable equivariant graph neural networks for the Hamiltonians of molecules and solids. *NPJ Comput. Mater.* **9**, 182 (2023).
15. Schutt, K. T., Gastegger, M., Tkatchenko, A., Muller, K. R. & Maurer, R. J. Unifying machine learning and quantum chemistry with a deep neural network for molecular wavefunctions. *Nat. Commun.* **10**, 5024 (2019).
16. Gong, X. et al. General framework for E(3)-equivariant neural network representation of density functional theory Hamiltonian. *Nat. Commun.* **14**, 2848 (2023).
17. Zhong, Y. et al. Universal machine learning Kohn-Sham Hamiltonian for materials. *Chin. Phys. Lett.* **41**, 077103 (2024).
18. Chen, K. Y. et al. Double superconducting dome and triple enhancement of T_c in the Kagome superconductor CsV_3Sb_5 under high pressure. *Phys. Rev. Lett.* **126**, 247001 (2021).
19. Zhang, Z. et al. Pressure-induced reemergence of superconductivity in the topological kagome metal CsV_3Sb_5 . *Phys. Rev. B* **103**, 224513 (2021).
20. Ozaki, T. Variationally optimized atomic orbitals for large-scale electronic structures. *Phys. Rev. B* **67**, 155108 (2003).
21. Ozaki, T. & Kino, H. Numerical atomic basis orbitals from H to Kr. *Phys. Rev. B* **69**, 195113 (2004).
22. Qin, X., Shang, H., Xiang, H., Li, Z. & Yang, J. HONPAS: a linear scaling open-source solution for large system simulations. *Int. J. Quantum Chem.* **115**, 647–655 (2014).
23. Luo, Z., Qin, X., Wan, L., Hu, W. & Yang, J. Parallel implementation of large-scale linear scaling density functional theory calculations with numerical atomic orbitals in HONPAS. *Front. Chem.* **8**, 589910 (2020).
24. Lin, P., Ren, X., Liu, X. & He, L. Ab initio electronic structure calculations based on numerical atomic orbitals: basic formalisms and recent progresses. *WIREs Comput. Mol. Sci.* **14**, e1687 (2023).
25. Chen, M., Guo, G. C. & He, L. Systematically improvable optimized atomic basis sets for ab initio calculations. *J. Phys. Condens. Matter* **22**, 445501 (2010).
26. Togo, A. First-principles phonon calculations with Phonopy and Phono3py. *J. Phys. Soc. Jpn* **92**, 012001 (2023).
27. Togo, A., Chaput, L., Tadano, T. & Tanaka, I. Implementation strategies in phonopy and phono3py. *J. Phys. Condens. Matter* **35**, 353001 (2023).
28. Giannozzi, P. et al. QUANTUM ESPRESSO: a modular and open-source software project for quantum simulations of materials. *J. Phys. Condens. Matter* **21**, 395502 (2009).
29. Giannozzi, P. et al. Advanced capabilities for materials modelling with Quantum ESPRESSO. *J. Phys. Condens. Matter* **29**, 465901 (2017).
30. Noffsinger, J. et al. EPW: A program for calculating the electron-phonon coupling using maximally localized Wannier functions. *Comput. Phys. Comm.* **181**, 2140–2148 (2010).
31. Zhou, J.-J. & Bernardi, M. Ab initioelectron mobility and polar phonon scattering in GaAs. *Phys. Rev. B* **94**, 201201 (2016).
32. Ma, J., Nessimagoudar, A. S. & Li, W. First-principles study of electron and hole mobilities of Si and GaAs. *Phys. Rev. B* **97**, 045201 (2018).
33. Zhou, J.-J. et al. Perturbo: a software package for ab initio electron-phonon interactions, charge transport and ultrafast dynamics. *Comput. Phys. Comm.* **264**, 107970 (2021).
34. Wang, Q. et al. Charge density wave orders and enhanced superconductivity under pressure in the Kagome metal CsV_3Sb_5 . *Adv. Mater.* **33**, e2102813 (2021).
35. Zheng, L. et al. Emergent charge order in pressurized Kagome superconductor CsV_3Sb_5 . *Nature* **611**, 682–687 (2022).
36. Ortiz, B. R. et al. CsV_3Sb_5 : A Z_2 topological Kagome metal with a superconducting ground state. *Phys. Rev. Lett.* **125**, 247002 (2020).
37. Tan, H., Liu, Y., Wang, Z. & Yan, B. Charge density waves and electronic properties of superconducting Kagome metals. *Phys. Rev. Lett.* **127**, 046401 (2021).
38. Zhang, J.-F., Liu, K. & Lu, Z.-Y. First-principles study of the double-dome superconductivity in the Kagome material CsV_3Sb_5 under pressure. *Phys. Rev. B* **104**, 195130 (2021).
39. Khan, F. S. & Allen, P. B. Deformation potentials and electron-phonon scattering: two new theorems. *Phys. Rev. B* **29**, 3341–3349 (1984).
40. Chen, X. et al. Highly robust reentrant superconductivity in CsV_3Sb_5 under pressure. *Chin. Phys. Lett.* **38**, 057402 (2021).
41. Poncé, S. et al. Temperature dependence of the electronic structure of semiconductors and insulators. *J. Chem. Phys.* **143**, 102813 (2015).
42. Poncé, S. et al. Temperature dependence of electronic eigenenergies in the adiabatic harmonic approximation. *Phys. Rev. B* **90**, 214304 (2014).
43. Blochl, P. E. The projector augmented wave (PAW) method: basics and applications. *Abstr. Pap. Am. Chem. S.* **217**, U690 (1999).
44. Kresse, G. & Joubert, D. From ultrasoft pseudopotentials to the projector augmented-wave method. *Phys. Rev. B* **59**, 1758–1775 (1999).
45. Zhong, Y. & Liu, S. Dataset for accelerating the calculation of electron-phonon coupling strength with machine learning. Zenodo <https://doi.org/10.5281/zenodo.11204268> (2024).
46. Zhong, Y. & Liu, S. Code for accelerating the calculation of electron-phonon coupling strength with machine learning. Zenodo <https://doi.org/10.5281/zenodo.12685941> (2024).
47. Abdullah, B. J. Size effect of band gap in semiconductor nanocrystals and nanostructures from density functional theory within HSE06. *Mater. Sci. Semicond. Process.* **137**, 106214 (2022).

Acknowledgements

We would like to express our gratitude to H. Shang and X. Qin for their valuable online discussions on the EPC and use of HONPAS. We acknowledge financial support from the Ministry of Science and Technology of the People's Republic of China (no. 2022YFA1402901, H.X.), NSFC (grant nos. 11991061, X.-G.G. and 12188101, H.X.), the Guangdong Major Project of the Basic and Applied Basic Research (Future functional materials under extreme conditions—2021B0301030005, H.X.), the Shanghai Science and Technology Program (no. 23JC1400900, H.X.) and the Shanghai Pilot Program for Basic Research – Fudan University 21TQ1400100 (no. 22TQ017, W.C.).

Author contributions

H.X. and J.-H.Y. proposed the research and the methodology in this work. Y.Z. and S.L. wrote the codes, performed the EPC calculation and wrote the paper. B.Z. conducted structure relaxation and phonon calculations for CsV_3Sb_5 . Z.T., Y.S. and W.C. checked the formulas and codes. H.X., J.-H.Y. and X.-G.G. revised the paper. All authors discussed the results.

Competing interests

The authors declare no competing interests.

Additional information

Supplementary information The online version contains supplementary material available at <https://doi.org/10.1038/s43588-024-00668-7>.

Correspondence and requests for materials should be addressed to Ji-Hui Yang or Hongjun Xiang.

Peer review information *Nature Computational Science* thanks Ting Cao, Yuan Ping and the other, anonymous, reviewer(s) for their contribution to the peer review of this work. Primary Handling Editor: Jie Pan, in collaboration with the *Nature Computational Science* team.

Reprints and permissions information is available at www.nature.com/reprints.

Publisher's note Springer Nature remains neutral with regard to jurisdictional claims in published maps and institutional affiliations.

Springer Nature or its licensor (e.g. a society or other partner) holds exclusive rights to this article under a publishing agreement with the author(s) or other rightsholder(s); author self-archiving of the accepted manuscript version of this article is solely governed by the terms of such publishing agreement and applicable law.

© The Author(s), under exclusive licence to Springer Nature America, Inc. 2024